Aerodynamic Investigation of a Convertible Tandem-Wing UAV Using Mid-Fidelity Numerical Simulations and Propeller Interaction Experimental Data

Javier Martínez-Lorenzo
Sergio Esteban
Universidad de Sevilla,
Departamento de Ingeniería Aeroespacial y Mecánica de Fluidos
Seville, Spain

Alessandro Cocco
Alberto Savino
Alex Zanotti
Politecnico di Milano,
Dipartimento di Scienze e Tecnologie Aerospaziali
Milan, Italy

ABSTRACT

This work investigates the aerodynamic interaction between front and rear propellers in a tandem-wing eVTOL UAV using combined wind tunnel testing and mid-fidelity simulations with the DUST solver. A comprehensive experimental campaign was conducted, varying key parameters such as relative propeller rotation, axial and lateral spacing, and freestream velocity. Thrust and power data were collected across hundreds of configurations, enabling an in-depth analysis of wake-induced effects on propeller efficiency. DUST simulations were used to predict the aerodynamic loads on the rear propeller, focusing on the same configurations and using the 13×6.5E blade geometry. The comparison between numerical and experimental thrust coefficients reveals promising agreement under most conditions, while discrepancies at high advance ratios highlight the need for more refined RPM control and extended test matrices. The study establishes a solid foundation for future aerodynamic optimization of distributed propulsion systems and hybrid tandem platforms for advanced aerial mobility.

NOTATION

C_T = propeller thrust coefficient
C_P = propeller power coefficient
D = propeller diameter
J = advance ratio
M = Mach number
n = propeller angular velocity
P = propeller power
Q = propeller torque
T = propeller thrust [N]
U_∞ = free-stream velocity
ρ = air density
η = propeller efficiency

INTRODUCTION

Urban Air Mobility (UAM) concepts have driven significant research efforts towards innovative rotorcraft configurations, particularly focusing on tiltrotors and convertible UAVs. The increasing demand for efficient vertical takeoff and landing (VTOL) systems has led to the exploration of tandem-wing UAVs, which combine fixed-wing efficiency with rotor-based maneuverability. However, these configurations introduce complex aerodynamic challenges, particularly in transition phases, where propeller-wing interactions and wake dynamics play a crucial role in performance (Ref. 1). Previous studies (Refs. 2–4) have investigated propeller-propeller interactions in eVTOL configurations, revealing significant performance losses due to wake impingement effects. Furthermore, research on mid-fidelity aerodynamic solvers has demonstrated their ability to capture vortex interactions in distributed propulsion systems (Refs. 2, 5, 6). Despite these advances, a detailed understanding of the aerodynamic coupling between tandem wings and propeller-induced downwash effects remains an open challenge.

This paper addresses this knowledge gap by integrating wind tunnel experiments with numerical simulations using the DUST mid-fidelity solver developed by POLIMI (Ref. 7) to investigate the aerodynamic behavior of a convertible tandem-wing UAV prototype. The UAV, currently under development at the Aerospace Engineering Department of University of

Seville, is designed for emergency response applications. This second generation prototype, named VERSATILE, is an evolution of the fixed-wing eVTOL aircraft developed under the ProVANT-EMERGENTIa project (Ref. 8), a joint effort between the University of Seville (US), the Federal University of Minas Gerais (UFMG) and the newly collaborated with Politecnico di Milano (POLIMI). The VERSATILE UAV features a challenging aerodynamic configuration, particularly due to the propeller-wing interactions arising from propellers mounted at the tips of the tandem wings (see Fig. 1). Understanding these aerodynamic and propulsive interactions is crucial for optimizing efficiency, stability, and transition flight dynamics in future search and rescue UAV missions.

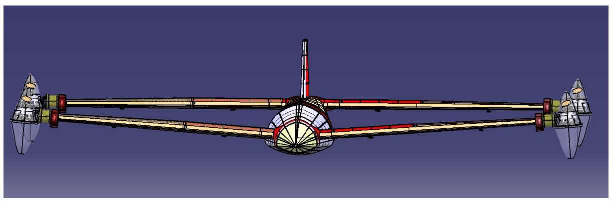

(a) Front view

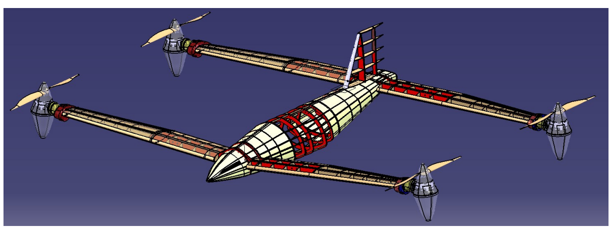

(b) Side view

Figure 1: Layout of the Tandem Wing VERSATILE Prototype

The objective of this study is to analyze the aerodynamic interactions between tandem propellers and tandem wings surfaces, combining wind tunnel experiments and mid-fidelity aerodynamic simulations using the DUST solver (Ref. 7). The approach builds on previous experimental studies that characterized performance variations in interacting propellers, expanding the analysis to a convertible UAV configuration where propeller-induced wake effects are particularly relevant. The methodology follows a twofold strategy:

1. Wind tunnel experiments provide direct measurements of propeller efficiency variations, wake-induced aerodynamic penalties, and the impact of propeller arrangement on thrust and energy consumption;

2. Numerical simulations using DUST replicate the experimental conditions, allowing for a detailed wake analysis and the quantification of aerodynamic coupling effects between propellers and the tandem wing.

The remainder of this paper is structured as follows. Section 2 describes the experimental campaign carried out at the University of Seville, including the test rig, parameter space, and postprocessing. Section 3 presents the wind tunnel results and discusses aerodynamic trends related to the overlap and swirl interaction of the propeller. Section 4 introduces the DUST solver and outlines the numerical strategy to simulate wake-induced aerodynamic interactions in the tandem wing configuration. Section 5 compares experimental and numerical results, highlighting key validation metrics and design insights. Finally, Section 6 provides conclusions and identifies areas for future research.

WIND TUNNEL EXPERIMENTS

A comprehensive wind tunnel campaign was carried out at the Aerospace Engineering Department of the University of Seville to investigate aerodynamic interactions between tandem propellers. The test rig allows for systematic variation of multiple key parameters, including propeller sense of rotation, spatial overlap, pitch settings, and RPM combinations, under different freestream velocities.

The goal was to evaluate the influence of these parameters on thrust generation and wake-induced interference, particularly in overlapping disk configurations. The study includes both co-rotating and counter-rotating setups at various longitudinal and transverse separations (see Figs. 2a and 2b).

While a broad experimental matrix was tested (see Section), the current analysis focuses on a subset of cases where:

- The same blade geometry (13x6.5E) is used for both propellers,

- Front and rear rotors operate at the same RPM,

- Only the thrust coefficient (C_T) is considered for comparison with numerical simulations.

This reduction facilitates clearer assessment of aerodynamic effects while avoiding confounding variables related to asymmetric loading or pitch differences. The detailed setup, instrumentation, and test matrix are described in Section .

METHODOLOGY

This section details the experimental methodology and data processing strategy. It includes a description of the wind tunnel facility, test bench components, the experimental matrix, and acquisition pipeline.

Experimental Setup and Parameters

Wind Tunnel Facility All tests were performed in the open loop subsonic wind tunnel ETSi, which provides flow velocities of approximately 30 m / s in a test section $1.4 \times 1.8 \times 5$, m. A nine-stage secondary electric fan array adjusts the speed of the tunnel. A built-in 3-axis positioner (Fig. 2a) permits moving the rear propeller in the longitudinal (X) and transverse (Y) directions, while the front propeller is fixed. For safety and repeatability, both tunnel doors remain closed during experiments.

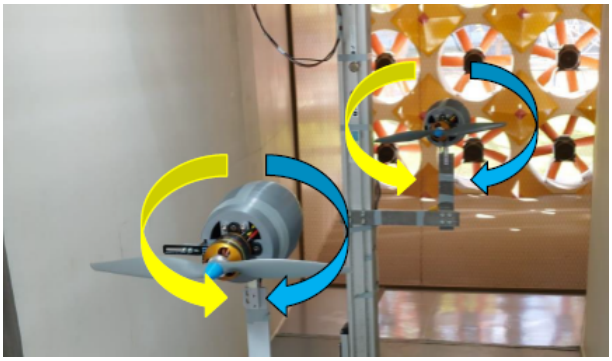

(a) Propellers set up in the US wind tunnel

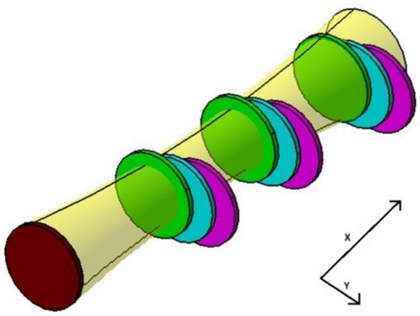

(b) Overlapping propellers combinations

Figure 2: Wind Tunnel Tandem Propellers Overlapping Set Up

Motor Stand and Electronics A Tyto Robotics *RC Benchmark Series 1585* (Ref. 9), test stand measures thrust and torque via load cells, along with voltage/current to determine mechanical and electrical power. Each stand includes the following:

- *Load cells*: calibrated for thrust (vertical mounting) and torque (horizontal).
- *ESC and PCB*: The Mezon 115 Opto ESC, developed by the company Jeti Model (Ref. 10), receives commands from the software (PWM), while the PCB logs all sensor readings (including an internal pitot or external sensor) and transmits them via USB.
- *Motor*: An AXI 4130/16 outrunner BLDC motor (Ref. 11) powers each propeller. For counterrotation, a pusher prop is substituted on the rear motor, reversing polarity.

The propellers used in the project belong to APC Propellers (Ref. 12), a company with extensive experience and a long-standing presence in the industry, and the following *Thin Electric* category propellers are selected: 13x4E, 13x6.5E & 14x10E.

A separate stand holds the front propeller in a fixed position near the wind tunnel inlet (to minimize upstream disturbance). The rear stand is mounted on the positioner, allowing for changes in the (X, Y) overlap.

Nacelle Fairing and Vibration Control Because exposed wires and bench components can distort the slipstream and introduce flow separation, a 3D printed nacelle encloses each motor, significantly reducing vibration (up to 65%) and improving the uniformity of the measured flow. The nacelle was designed in accordance with the simplified guidelines presented in Zanenga's Ph.D. thesis (Ref. 13).

Test Matrix and Acquisition Protocol

The experimental campaign was designed to investigate the influence of multiple physical parameters on the aerodynamic performance of overlapping tandem propellers. To capture a wide range of interaction effects while maintaining feasibility within the available wind tunnel time, a structured matrix of configurations was defined. This matrix includes variations in rotation sense, geometric separation, blade pitch, freestream velocity, and rotor speeds.

The six main parameters studied in the campaign are summarized as follows:

- **Sense of rotation**: same (S) vs. counter (C).
- **Freestream velocity**: 0, 5, 10 m/s.
- **X-separation**: 60, 110, 160 cm.
- **Y-separation**: 0 cm, 8.25 cm (D/4), 16.5 cm (D/2).
- **Pitch**: $4''$, $6.5''$, $10''$ for both front/rear.
- **RPMs**: 2000–8000 (4×4 matrix).

where D represents the diameter of the propeller ($13''$). Each configuration yields 16 subcases per wind speed. Reference tests were conducted with only the rear propeller active, to isolate baseline thrust and power.

Discrete Speed Sweeps and Filtering RPM commands were applied via stepwise PWM scripts on both stands. For each point:

- Data collected at 40 Hz for 1 s (approx. 40 samples).
- Automatic outlier removal via JavaScript filtering.
- Only averaged values saved in the .csv files.

Each saved point includes a 95% confidence interval based on the remaining filtered data. This process reduces post-processing time but prevents recovering the number of rejected samples or raw statistical spread. Its implications are discussed in the following subsection.

Confidence Interval and Data Filtering Methodology

Each wind tunnel measurement was conducted over a period of 10 seconds, with data sampled at a frequency of 40 Hz. This setup yields approximately 400 raw data points per test case, capturing thrust, torque, voltage, and current signals. However, to ensure signal stability, the first 3 seconds following each change in RPM setpoint were excluded from the analysis to allow the system to reach steady state. Similarly, the final 3 seconds of each window were discarded to avoid any undesired artifacts linked to control system transitions or edge effects.

Thus, only the central 4 seconds of the acquisition (160 samples) were retained for post-processing. Within this window, the embedded JavaScript control software performed automatic filtering and data conditioning as follows:

- Outliers were identified and removed in real time from the raw sample stream.
- The mean value was computed from the remaining valid data points.
- A 95% confidence interval was calculated based on the cleaned sample distribution.

This strategy significantly reduced post-processing overhead and data storage demands — only one averaged, filtered value per measurement was saved to the output `.csv` file, along with its corresponding confidence range.

Nevertheless, this automated approach imposes certain limitations:

- The full time history is not retained, preventing later inspection or custom reprocessing.
- The internal logic for outlier detection is fixed and opaque, limiting traceability.
- The statistical output consists of a single averaged value, with no detailed histogram or record of sample dispersion beyond the reported confidence interval.

Despite these limitations, the resulting dataset provides statistically sound values, capturing the steady-state behavior of the system under each tested condition. The reported 95% confidence intervals reflect the internal variability and help support the comparative analysis against numerical predictions.

Interpolation An essential decision was *not* to interpolate C_T, C_P directly on the discrete points, but rather to interpolate base thrust and torque first. With only $\approx 3-4$ points per test in J, direct polynomial fits to $C_T(J)$ proved unreliable. Instead, we found a more stable ridge-regression fit in RPM-$\{T,Q\}$ space, then used standard formulas:

$$C_T = \frac{T}{\rho n^2 D^4}, \quad C_P = \frac{P}{\rho n^3 D^5}, \quad J = \frac{U_\infty}{nD}, \quad \eta = \frac{Q \cdot n}{T \cdot V}$$

with partial corrections for compressibility as suggested by the Prandtl transformation: $J = J^i \sqrt{1-M_\infty^2}$, and C_T, C_P scaled accordingly.

$$C_T = \frac{C_T^i(D)}{(1-M_\infty^2)^{\frac{5}{2}}}, \quad C_P = \frac{C_P^i(D)}{(1-M_\infty^2)^3},$$

where M_∞ is determined by the vectorial result of tangential and transverse air velocities at 75% of the root on the blade. Therefore:

$$M_\infty = \frac{\sqrt{\left(\frac{3}{4}\frac{D}{2}\Omega\right)^2 + V_\infty^2}}{\sqrt{\gamma R_g T}} \tag{1}$$

with Ω is the rotational speed of the propeller, V_∞ is the flow velocity, and $\sqrt{\gamma R_g T}$ is the speed of sound under corresponding conditions.

Data Representation

To systematically explore how propeller performance varies with overlap and inflow conditions, a large number of configurations were tested. Each case yields up to 9 data points (3 wind tunnel velocities $\times$ 3 RPM levels). For plotting purposes, we fix one or two parameters at a time (typically the front propeller pitch and the spatial overlap configuration (X,Y)), and represent thrust coefficient (C_T), power coefficient (C_P), and propeller efficiency (η) as a function of the advance ratio J.

The advance ratio J is computed from each test's instantaneous wind speed and rear propeller RPM. However even if two different combinations of U_∞ and RPM yield the same J, the resulting C_T can differ. This is due to the nonlinear dependence of thrust on both RPM and freestream velocity, particularly at low RPMs. Although we applied a Prandtl–Glauert compressibility correction, in our case it did not collapse the CT–J curves as effectively as in previous works. For this reason, and to avoid confusion, the final version of the manuscript includes only the 10 m/s wind tunnel curves in the CT–J plots used for DUST comparisons. Figures 3 and 4 illustrates the results in terms of thrust and power coefficient against advance ratio.

WIND TUNNEL RESULTS

This section presents the main findings of our experimental and numerical study on overlapping propellers. While the full test campaign includes hundreds of configurations covering a broad range of parameters (rotational sense, spacing, pitch, and RPM combinations), we restrict our analysis here to a representative subset that matches the conditions simulated in DUST.

Specifically, we focus on cases where both front and rear propellers use the 13x6.5E geometry and operate at the same

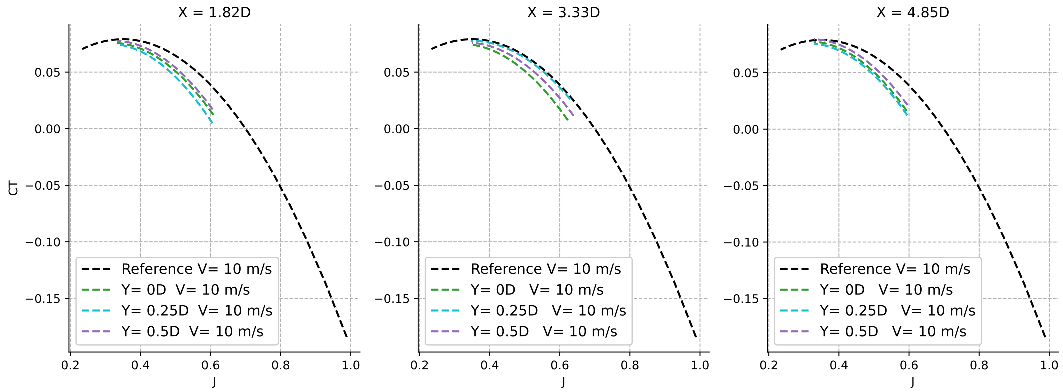

Figure 3: Example of C_T–J curve representation for different lateral spacings at fixed longitudinal positions.

RPM, to ensure direct comparability and minimize confounding effects due to asymmetric loading or variable inflow. Although results were experimentally obtained for thrust coefficient (C_T), power coefficient (C_P), and efficiency (η), only C_T is used in the comparison with DUST predictions.

The general trends, are reported in Figures 3 and Figure 4. Both figures refer to co-rotating propeller configurations and are extracted from the larger experimental dataset. The C_P results are only included for context, helping to explain the power demand associated with overlapping operation, but are not part of the numerical validation effort in this paper.

The following sections discuss how overlap influences the thrust coefficient (C_T), power coefficient (C_P). We first focus on the same sense rotation of the front and rear propellers, then move to counter-rotating case.

Co-Rotating

Regarding C_T, our data indicate that increasing wind speed, front rotational speed, or front pitch consistently results in a decrease in C_T (as expected, since C_T generally decreases with increasing advance ratio, J). This effect is especially pronounced when the back propeller is operating at a lower pitch. Thus, the basic conclusion is that an overlapped configuration is typically detrimental to performance.

Considering the torque coefficient, When both propellers rotate in the same direction, the rear propeller benefits from a reduced torque load, thereby lowering its power coefficient (C_P). This reduction occurs because the swirling airflow from the front propeller partially drives the rear blades. However, if either propeller stalls—especially when the back propeller operates at a high pitch (e.g. 10”),C_P can increase abruptly.

Moreover, our findings indicate that the asymmetry in the inflow is the key factor that governs C_P. In regions where part of the rear propeller is immersed in the slipstream of the front propeller while other parts are not, the C_P values are significantly higher. For configurations with smaller throat diameters (resulting from low pitch or low front RPM), these elevated C_P values appear closer to the propeller axis. In contrast, at higher throat diameters (associated with high pitch or high front RPM), the regions of increased C_P shift further from the axis. This is clearly illustrated in Figure 4, where the values C_P for the equiaxial propeller (shown in pink) remain consistently higher compared to the other two Y configurations.

In summary, while overlapping propellers with the same sense of rotation may show theoretical benefits under narrowly defined conditions, the configuration is generally unattractive. Small parameter variations can quickly shift any potential benefits into pronounced negative effects. For aircrafts that must operate across a wide range of free-stream velocities (U_∞) and mission profiles, it is preferable to position the back propeller outside the front slipstream. Although certain specialized scenarios may exploit the advantages of overlapping configurations, such benefits are too narrowly constrained to be practical for general applications.

Counter-Rotating

In principle, a counter-rotating back propeller can recover the swirl from the front prop, converting it into useful thrust. Although benefits were observed at minimal axial spacings, which is consistent with the findings reported in the literature (Ref. 14), typical gaps did not produce major thrust improvements. Instead, asymmetries and turbulence often undermined any advantage of swirl recovery.

Because the rear prop rotation is reversed relative to the incoming swirl, C_P is often higher. Thrust C_T can be somewhat more steady than in the same sense rotation, although overall net benefits remain modest unless the spacing is very small.

As in the same-sense cases, only thrust coefficient (C_T) data are considered for comparison with DUST, while the C_P trends provide context for interpreting flow-induced load variations.

NUMERICAL SIMULATIONS

DUST mid-fidelity solver

Numerical simulations of the tandem propellers configurations investigated by experiments were performed using the

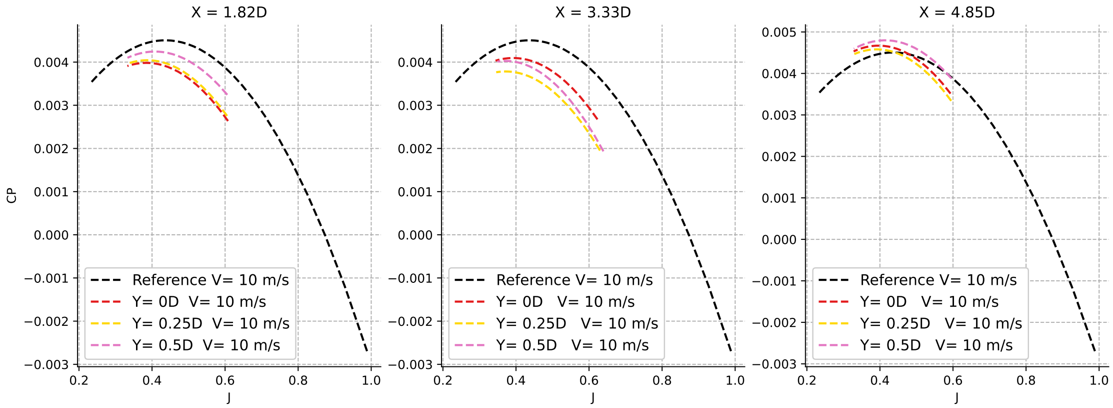

Figure 4: C_P–J curve representation for different lateral spacings at fixed longitudinal positions.

mid-fidelity aerodynamic solver DUST, developed by Politecnico di Milano (Ref. 7). The implementation of DUST exploits the Object Oriented paradigms of the latest Fortran standards to obtain the desired level of flexibility in modelling an aircraft potentially composed of several components and describing their motion. The aerodynamic solver relies on the Helmholtz decomposition of the velocity field, $\vec{u} = \vec{u}_\varphi + \vec{u}_\psi$, being $\vec{u}_\varphi$ and $\vec{u}_\psi$ the irrotational and solenoidal contributions respectively. The solution is advanced in time using a time-stepping algorithm that alternates the solution of a three-dimensional boundary element method for $\vec{u}_\varphi$ and the Lagrangian evolution in time of the rotational part of the velocity $\vec{u}_\psi$. Only the surface mesh of the model is required and different aerodynamic elements allow for different levels of fidelity in the model, ranging from lifting line elements (Refs. 15, 16) to zero-thickness lifting surfaces and surface panels (Ref. 17). In particular, one-dimensional lifting line elements are used for a proper modelling of lifting bodies with high aspect ratio as blades. These elements naturally represent viscous effects, since they rely on tabulated aerodynamic lift, drag and moment coefficients of two-dimensional sections as functions of the relative velocity direction and magnitude. This numerical tool, based on the use of VPM for wake modelling (Refs. 18, 19), was thoroughly validated against experiments and high fidelity CFD for interactional aerodynamics rotorcraft applications (Refs. 1–3). DUST can be considered in a mature state to be used for an accurate investigation of multirotors aerodynamic interactions.

In this preliminary work, the main objective is to validate the numerical predictions against experimental data, ensuring consistency between predicted wake structures and observed aerodynamic performance. By integrating DUST's wake modeling capabilities with experimental thrust and efficiency measurements, the study will develop quantitative metrics that link propeller interactions to electric motor performance. Ultimately, this approach enhances DUST's predictive capabilities, allowing it to simulate aerodynamic interactions between propellers and wings in tandem UAVs, quantify efficiency losses or gains due to wake-induced aerodynamic effects, and provide design insights for future convertible UAV configurations, optimizing propeller placement for improved thrust efficiency and energy consumption.

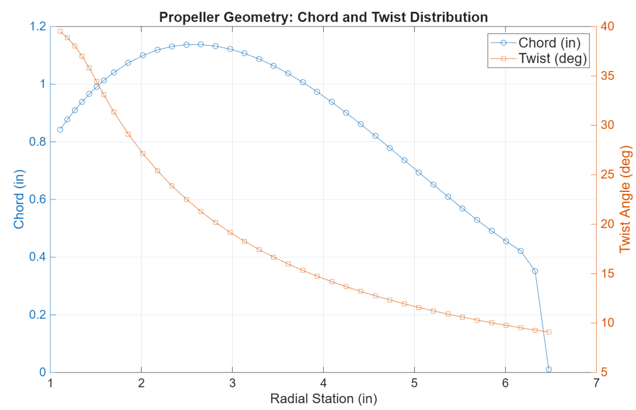

Figure 5: Propeller Geometry for Numerical Setup for APC 13x6.5.

Numerical model

The propeller geometry implemented in the DUST simulations corresponds to the commercially available APC 13x65E model, which is widely used in small and medium UAV platforms. Figure 5 shows the radial distribution of the chord length and the twist angle for this propeller.

The aerodynamic section used by APC in this model is based on a modified Clark-Y airfoil, optimized for low Reynolds number applications. It offers a compromise between high static thrust performance and power efficiency, making it suitable for hovering and forward flight conditions.

The model includes only the surface mesh of the propeller blades. These blades are represented using 25 lifting-line elements for each blade, enabling load corrections through aerodynamic lookup tables that incorporate viscous and compressibility effects. The aerodynamic coefficient tables for the blade airfoils were generated using NeuralFoil (Ref. 20), an XFoil-trained tool. The DUST model with the particle wake is shown in Figure 6.

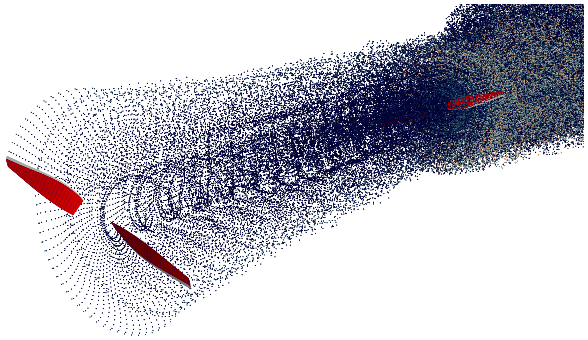

Figure 6: DUST model with particle wake visualization

Each simulation consists of 30 complete rotor revolutions, with a time step corresponding to 72 step-per-rev in order to achieve convergence.

RESULTS AND DISCUSSION

In table 1 are reported the ranges of the conditions considered for the current work. All combinations within the parameters were considered except the RPM one, in which the same propeller speed was set for both propellers.

Table 1: Test matrix summary for tandem propeller configurations.

Configuration	RPM	Δx [m]	Δy [m]
Co / Counter	2000–8000	0.6–1.6	0.0–0.17

Co-Rotating Configuration

To evaluate the predictive accuracy of the DUST solver, a systematic comparison was performed between numerical simulations and wind tunnel measurements for nine co-rotating configurations, where both propellers rotate in the same direction. All cases were conducted at a fixed freestream velocity of $U_\infty = 10$ m/s to ensure consistency. Each configuration varies in terms of the longitudinal separation (Δx) and the lateral offset (Δy) between the front and rear propellers.

The results are presented in a 3×3 matrix in Fig. 7, where each subplot corresponds to a unique combination of Δx and Δy. The layout is organized such that:

- Each **row** corresponds to a fixed longitudinal separation Δx, with increasing values from top to bottom: $\Delta x =$ 0.6 m, 1.1 m, and 1.6 m (approximately 1.8D, 3.3D, and 4.8D).
- Each **column** corresponds to a fixed lateral offset Δy, with increasing values from left to right: $\Delta y = 0.0$ m, 0.0825 m ($D/4$), and 0.165 m ($D/2$).

Each subplot shows the rear propeller thrust coefficient C_T as a function of advance ratio J, allowing a direct evaluation of wake-induced aerodynamic interaction across varying spatial separations.

In general, DUST follows the expected trend of decreasing C_T with increasing J, and in many cases, it aligns closely with the experimental curves. Notably, in configurations with larger longitudinal and lateral separations (e.g., Figures 7d, 7i, the agreement between numerical and experimental data is strong in both trend and magnitude.

However, in some overlapping cases (e.g., Figures 7b, 7f), both DUST and experiments exhibit non-classical curvature near $J = 0.4$–0.5. DUST retains a smooth concavity, while the experimental curves flatten or slightly invert, a behavior not typical of isolated propeller performance. These deviations could stem from the combined effects of wake interference and experimental resolution limits.

At high J (low RPM), DUST predicts negative C_T, consistent with possible windmilling or drag conditions. Experimental data show C_T values approaching zero or slightly negative as well. These regimes are more sensitive and could benefit from finer RPM sampling in future campaigns.

Counter-Rotating Configuration

Figure 8 shows rear propeller C_T vs. J in counter-rotation scenarios. For simplicity, only the interaction case is shown (DUST vs. experiment); isolated rear propeller data are not displayed, although they were measured.

In these configurations, discrepancies between numerical and experimental results appear slightly more pronounced than in the same-sense cases. Nevertheless, DUST maintains the general C_T decreasing trend with J, and curve shapes remain physically reasonable.

Overall, results highlight the value of combining experimental and numerical approaches to better understand propeller interference in tandem layouts.

Comparative Trends: Co-Rotating vs. Counter-Rotating

While Figs. 7 and 8 provide a comprehensive grid of all tested configurations in matrix form, they can be visually dense and may obscure certain patterns of aerodynamic interaction. To better isolate and interpret key effects, we complement those grids with targeted comparative plots.

These new figures aim to highlight how rear propeller performance varies when either longitudinal (Δx) or lateral (Δy) spacing is modified—under both co-rotating and counter-rotating conditions. Each subplot presents the thrust coefficient C_T of the rear propeller as a function of the advance ratio J, enabling direct visual comparison of the rotational regimes.

The following subsets were selected to illustrate these effects:

- **Co-rotating regime:** $\Delta y = 0.08$ m fixed, varying $\Delta x = \{0.6, 1.1, 1.6\}$ m — showing how increasing axial separation impacts wake interference (Fig. 9).

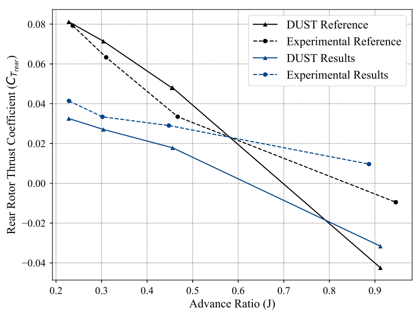

(a) $\Delta x = 0.6$, $\Delta y = 0.0$

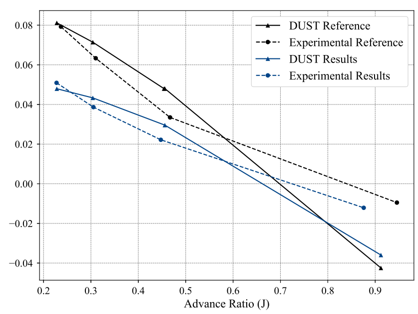

(b) $\Delta x = 0.6$, $\Delta y = 0.08$

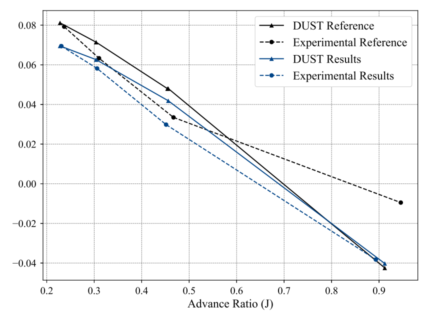

(c) $\Delta x = 0.6$, $\Delta y = 0.17$

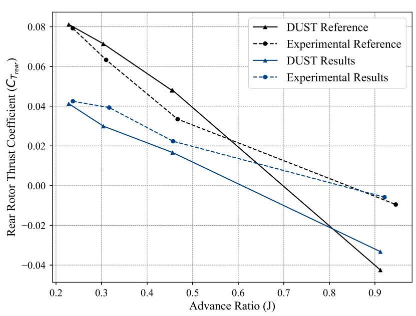

(d) $\Delta x = 1.1$, $\Delta y = 0.0$

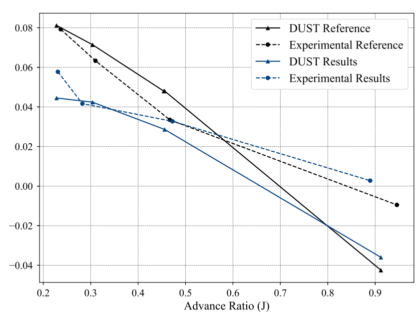

(e) $\Delta x = 1.1$, $\Delta y = 0.08$

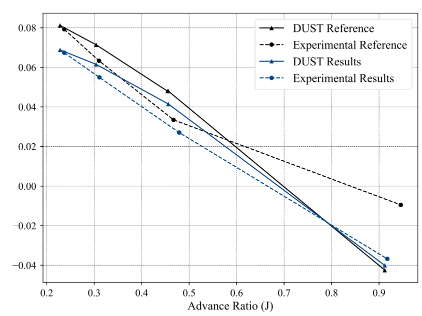

(f) $\Delta x = 1.1$, $\Delta y = 0.17$

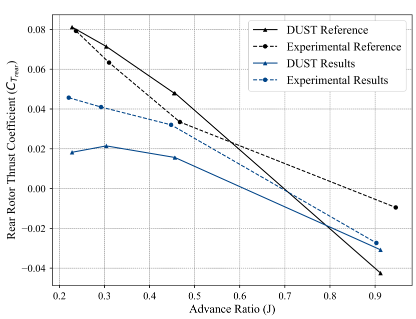

(g) $\Delta x = 1.6$, $\Delta y = 0.0$

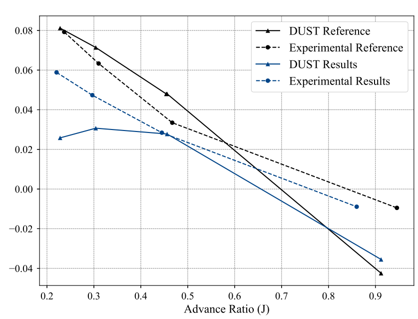

(h) $\Delta x = 1.6$, $\Delta y = 0.08$

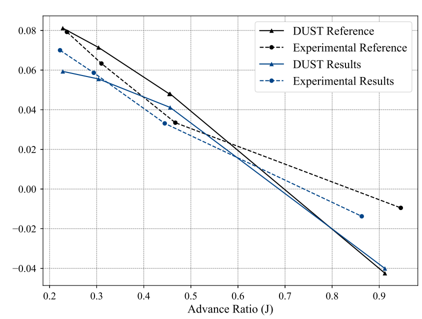

(i) $\Delta x = 1.6$, $\Delta y = 0.17$

Figure 7: Rear propeller thrust coefficient C_T vs. advance ratio J for a series of tandem propeller configurations with varying spatial overlap. Each subplot presents a comparison between experimental and DUST simulation results.

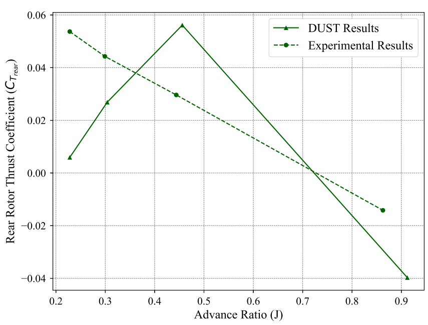

(a) $\Delta x = 0.6$, $\Delta y = 0.0$

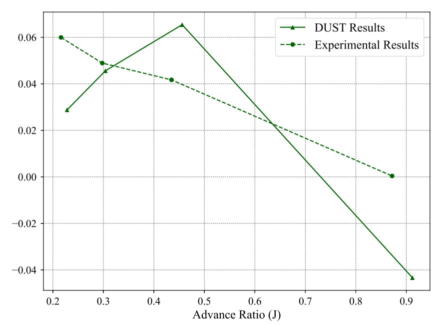

(b) $\Delta x = 0.6$, $\Delta y = 0.08$

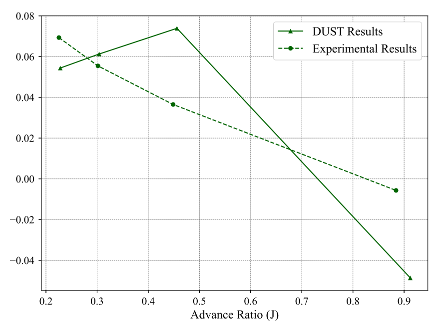

(c) $\Delta x = 0.6$, $\Delta y = 0.17$

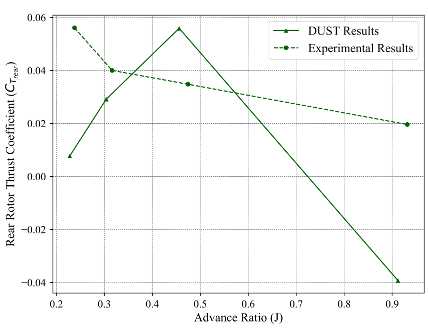

(d) $\Delta x = 1.1$, $\Delta y = 0.0$

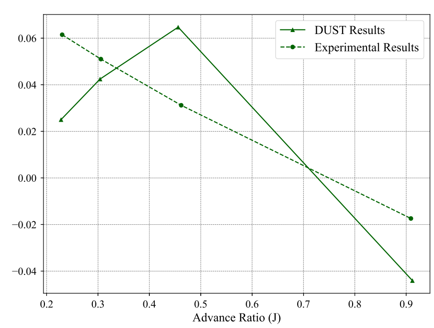

(e) $\Delta x = 1.1$, $\Delta y = 0.08$

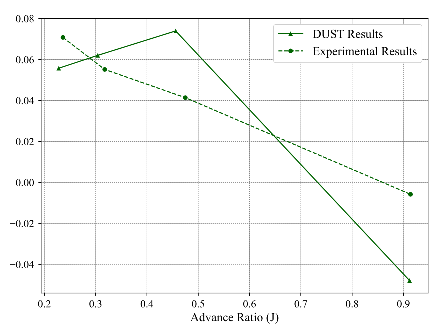

(f) $\Delta x = 1.1$, $\Delta y = 0.17$

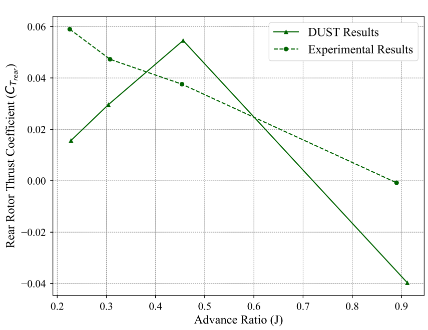

(g) $\Delta x = 1.6$, $\Delta y = 0.0$

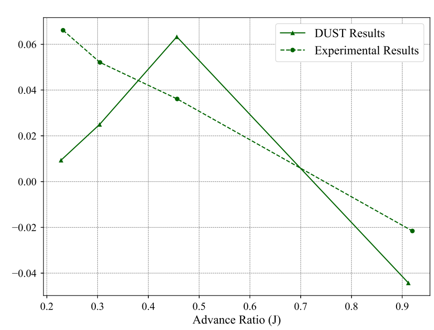

(h) $\Delta x = 1.6$, $\Delta y = 0.08$

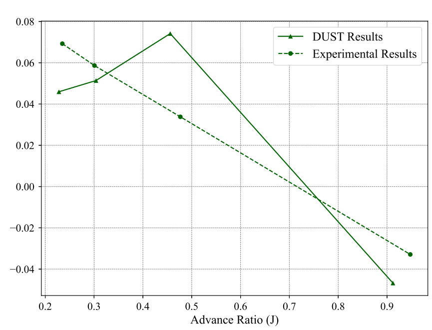

(i) $\Delta x = 1.6$, $\Delta y = 0.17$

Figure 8: Rear rotor thrust coefficient C_T vs. advance ratio J, for counter rotating configuration.

- **Counter-rotating regime:** $\Delta x = 1.1$ m fixed, varying $\Delta y = \{0.00, 0.08, 0.17\}$ m — highlighting the influence of lateral displacement on swirl recovery and rear prop efficiency (Fig. 10).

For each configuration, both experimental (Figs. 9a and 10a) and DUST (Figs. 9b and 10b) data are shown separately to avoid visual clutter. All curves include the isolated rear propeller as a baseline (solid black). Co-rotation results appear as solid lines, while dashed lines indicate counter-rotation.

These focused comparisons help clarify how thrust performance evolves across typical operational configurations, and provide an intuitive framework to interpret the more detailed matrix figures. They also enable a more precise discussion of wake alignment and swirl interaction phenomena between rotational regimes.

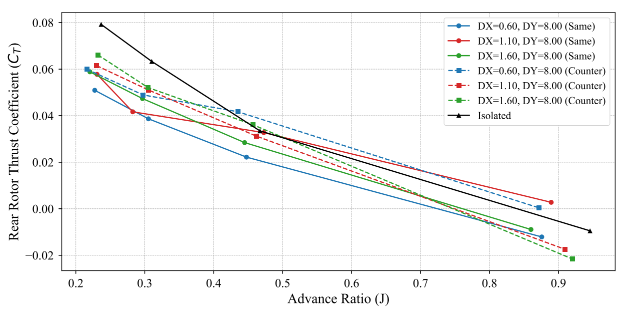

(a) Experimental Results

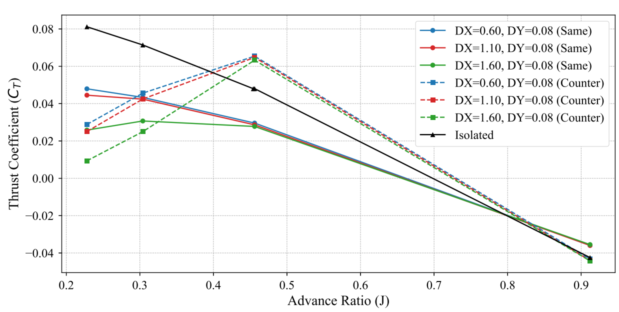

(b) DUST Simulations

Figure 9: Rear propeller C_T vs. J for experimental co-rotating configurations with fixed $\Delta y = 0.08$ m and varying Δx. Solid lines represent co-rotation and dashed lines represent counter-rotating, and black solid the isolated baseline.

Global correlation analysis

To quantify the level of agreement between the DUST simulations and the experimental measurements, two standard error metrics were computed for each configuration:

- **Mean Absolute Error (MAE)**: This metric captures the average magnitude of deviations between experimental and numerical data. It is computed as:

$$\text{MAE} = \frac{1}{N}\sum_{i=1}^{N}\left|C_{\text{T}}^{\text{DUST}}{}_{i} - C_{\text{T}}^{\text{EXP}}{}_{i}\right|$$

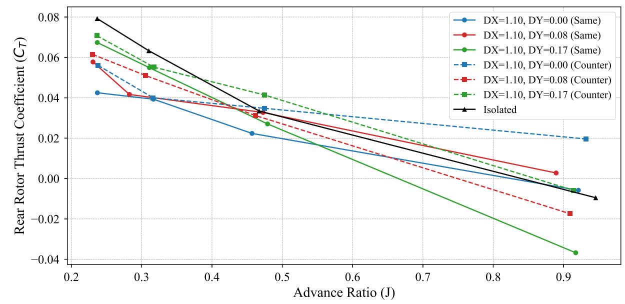

(a) Experimental Results

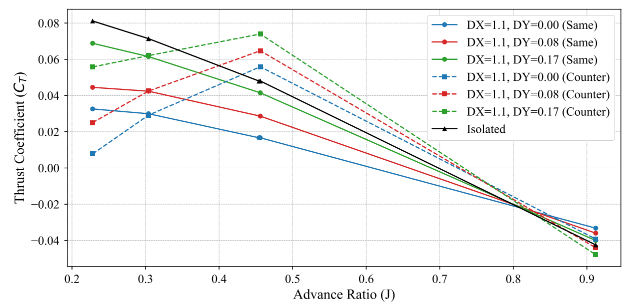

(b) DUST Simulations

Figure 10: Rear propeller C_T vs. J for experimental co-rotating configurations with fixed $\Delta x = 1.10$ m and varying Δy. Solid lines represent co-rotation and dashed lines represent counter-rotating, and black solid the isolated baseline.

- **Root Mean Squared Error (RMSE)**: This indicator penalizes larger deviations more strongly and highlights outliers or nonlinear mismatches. It is defined as:

$$\text{RMSE} = \sqrt{\frac{1}{N}\sum_{i=1}^{N}\left(C_{\text{T}}^{\text{DUST}}{}_{i} - C_{\text{T}}^{\text{EXP}}{}_{i}\right)^2}$$

Both metrics were calculated using Python scripts based on NumPy routines. For each test condition, the experimental and numerical values of rear propeller thrust coefficient (C_{T}) were paired by advance ratio J, and the error computed over all available points (see Table2).

Table 2: Comparison of MAE and MSE values for DUST vs. experimental data in Same Sense and Counter-Rotating configurations at $U_\infty = 10$ m/s.

Spacing		**Co-Rotating**		**Counter-Rotating**	
Δx [m]	Δy [m]	**MAE**	**MSE**	**MAE**	**MSE**
0.6	0.00	0.0293	0.0314	0.0169	0.0221
0.6	0.08	0.0255	0.0294	0.0097	0.0128
0.6	0.17	0.0253	0.0296	0.0046	0.0065
1.1	0.00	0.0348	0.0399	0.0109	0.0148
1.1	0.08	0.0263	0.0284	0.0142	0.0206
1.1	0.17	0.0241	0.0279	0.0064	0.0081
1.6	0.00	0.0292	0.0316	0.0167	0.0188
1.6	0.08	0.0334	0.0361	0.0192	0.0228
1.6	0.17	0.0212	0.0246	0.0120	0.0148

Note: While DUST simulations precisely impose the same RPMs on both front and rear propellers, in the experimental setup the rear propeller RPM was not directly controlled and only the PWM signal was set. As a result, under varying aerodynamic load conditions (especially when wake interaction is present), slight deviations in RPM can occur, leading to small shifts in J and consequently in C_{T}. These discrepancies should be considered when interpreting the error metrics.

CONCLUSION AND FUTURE WORK

This work presents a joint experimental and numerical investigation of aerodynamic interactions in a tandem-propeller configuration, focusing on both same-sense and counter-rotating cases. DUST simulations and wind tunnel data were compared across a range of separation distances and RPM combinations.

In most configurations, the numerical model captured the expected trends and magnitudes of C_T, especially at low to mid J. Some deviations were observed in more tightly coupled or counter-rotating setups, yet the source of these discrepancies remains unclear, and may stem from both modeling assumptions and experimental limitations.

Several factors may contribute to discrepancies:

- Experimental uncertainties in rear RPM control due to PWM load coupling;
- Measurement resolution and sensor filtering at high J;
- Absence of nacelle modeling in DUST (present in experiments).

These cases alone are not sufficient to challenge the robustness of the solver, which has demonstrated high fidelity in prior validated studies involving tandem configurations. Our results underline the need for:

- Extended wind tunnel campaigns to resolve sensitive J regions with more intermediate RPMs;
- Joint evaluation of solver predictions with known experimental uncertainty ranges;
- Balanced validation strategies that consider modeling assumptions and physical test limitations;
- Design more detailed and high-resolution experimental campaigns to isolate flow structures and better quantify wake-induced phenomena;
- Develop time-resolved measurements of wake interaction effects to provide reference datasets beyond steady-state performance;
- Reduce reliance on simulation-only diagnostics by enhancing the fidelity and repeatability of experimental setups, especially for transient and asymmetric flow cases;
- Perform repeatability analysis and RPM tracking to quantify variability in control input response (e.g., PWM to RPM transfer).

Future work will explore enriched test matrices, improved inflow characterization, and possibly hybrid data-driven techniques to assist in interpreting complex interference patterns.

Overall, this study highlights the importance of integrated experimental–numerical campaigns, where improving both the physical test protocols and the simulation configuration can mutually enhance model validation and understanding of complex aerodynamic interactions.

REFERENCES

1. Alex Zanotti, Alessandro Velo, Chiara Pepe, Alberto Savino, Donato Grassi, and Luca Riccobene. Aerodynamic interaction between tandem propellers in evtol transition flight configurations. *Aerospace Science and Technology*, 147:109017, 2024.

2. Alex Zanotti and Davide Algarotti. Aerodynamic interaction between tandem overlapping propellers in evtol airplane mode flight condition. *Aerospace Science and Technology*, 124:107518, 2022.

3. Daniele Granata, Alberto Savino, Donato Grassi, Luca Riccobene, and Alex Zanotti. Aerodynamic and aeroacoustics investigation of tandem propellers in hover for evtol configurations. *Aerospace Science and Technology*, 155:109740, 2024.

4. Jinggen Zhao and Chengjian He. Real-time simulation of coaxial rotor configurations with combined finite state dynamic wake and vpm. In *Annual Forum Proceedings - AHS International*, volume 3, 05 2014.

5. Eduardo Alvarez and Andrew Ning. Development of a vortex particle code for the modeling of wake interaction in distributed propulsion. In *AIAA Applied Aerodynamics Conference, Atlanta, GA*, 06 2018.

6. J. Tan, Y. Sun, and G. N. Barakos. Unsteady loads for coaxial rotors in forward flight computed using a vortex particle method. *The Aeronautical Journal*, 122(1251):693–714, 2018.

7. Matteo Tugnoli, Davide Montagnani, Monica Syal, Giovanni Droandi, and Alex Zanotti. Mid-fidelity approach to aerodynamic simulations of unconventional vtol aircraft configurations. *Aerospace Science and Technology*, 115:106804, 2021.

8. Samuel Torres Haro and Sergio Esteban. Parametric aerodynamic study of a convertible aircraft using cfd tools. provant emergentia project. In Ebrahim Samer El'Youssef, Mohammad Osman Tokhi, Manuel F. Silva 0001, and Leonardo Mejia Rincon, editors, *Synergetic*

Cooperation Between Robots and Humans - Proceedings of the CLAWAR 2023 Conference - Volume 1, Florianópolis, Brazil, 2-4 October 2023, volume 810 of *Lecture Notes in Networks and Systems*, pages 141–153. Springer, 2023.

9. Tyto Robotics. Series 1585 test stand documentation. https://www.tytorobotics.com/pages/series-1580-1585 [Accessed: 2025-05-30].

10. Jeti Model. Mezon 115 opto documentation. https://www.jetimodel.com/katalog/mezon-115-opto.htm [Accessed: 2025-05-30].

11. AXI Motors. Axi motors documentation, model motors. https://www.modelmotors.cz/about-axi/ [Accessed: 2025-05-30].

12. APC Propellers. Apc propellers technical information. https://www.apcprop.com/technical-information/?v=cd32106bcb6d [Accessed: 2025-05-30].

13. Erminio Samuele Zanenga. *Design and Engineering Methods for Open-Rotor Nacelle Shaping*. PhD thesis, Cranfield University, 2010.

14. Peter Schimming. Counter rotating fans - an aircraft propulsion for the future? *Journal of Thermal Science*, 12:97–103, 05 2003.

15. S Gallay and E Laurendeau. Nonlinear generalized lifting-line coupling algorithms for pre/poststall flows. *AIAA Journal*, 53(7):1784–1792, 2015.

16. Stanley T Piszkin and ES Levinsky. Nonlinear lifting line theory for predicting stalling instabilities on wings of moderate aspect ratio. Technical report, GENERAL DYNAMICS SAN DIEGO CA CONVAIR DIV, 1976.

17. Luigi Morino and Ching-Chiang Kuot. Subsonic potential aerodynamics for complex configurations: a general theory. *AIAA Journal*, 12(2):191–197, 1974.

18. Georges-Henri Cottet, Petros D Koumoutsakos, D Petros, et al. *Vortex methods: theory and practice*. Cambridge University Press, 2000.

19. Gregoire Stephane Winckelmans. *Topics in vortex methods for the computation of three-and two-dimensional incompressible unsteady flows*. PhD thesis, California Institute of Technology, 1989.

20. Peter Sharpe. NeuralFoil: An airfoil aerodynamics analysis tool using physics-informed machine learning. https://github.com/peterdsharpe/NeuralFoil, 2023.

CLASSIFICATION & COPYRIGHT